JACS
JOURNAL OF THE AMERICAN CHEMICAL SOCIETY

pubs.acs.org/JACS

Article

Intrinsic Activity of Metal Centers in Metal−Nitrogen−Carbon Single-Atom Catalysts for Hydrogen Peroxide Synthesis

Chang Liu,[‖] Hao Li,[‖] Fei Liu,[‖] Junsheng Chen, Zixun Yu, Ziwen Yuan, Chaojun Wang, Huiling Zheng, Graeme Henkelman,* Li Wei,* and Yuan Chen*

Cite This: *J. Am. Chem. Soc.* 2020, 142, 21861−21871

Read Online

ACCESS | Metrics & More | Article Recommendations | Supporting Information

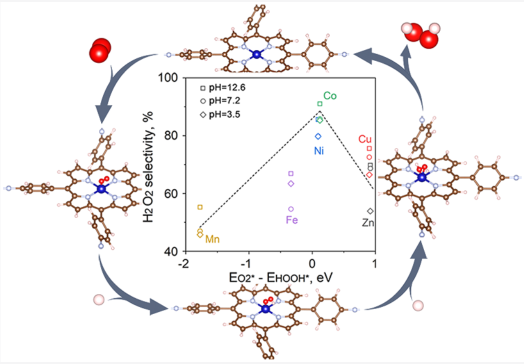

ABSTRACT: Metal−nitrogen−carbon (M−N−C) single-atom catalysts (SACs) show high catalytic activity for many important chemical reactions. However, an understanding of their intrinsic catalytic activity remains ambiguous because of the lack of well-defined atomic structure control in current M−N−C SACs. Here, we use covalent organic framework SACs with an identical metal coordination environment as model catalysts to elucidate the intrinsic catalytic activity of various metal centers in M−N−C SACs. A pH-universal activity trend is discovered among six 3d transition metals for hydrogen peroxide (H_2O_2) synthesis, with Co having the highest catalytic activity. Using density functional calculations to access a total of 18 metal species, we demonstrate that the difference in the binding energy of O_2* and HOOH* intermediates ($E_{O_2*} - E_{HOOH*}$) on single metal centers is a reliable thermodynamic descriptor to predict the catalytic activity of the metal centers. The predicted high activity of Ir centers from the descriptor is further validated experimentally. This work suggests a class of structurally defined model catalysts and clear mechanistic principles for metal centers of M−N−C SACs in H_2O_2 synthesis, which may be further extendable to other reactions.

1. INTRODUCTION

Single-atom catalysts (SACs) typically refer to heterogeneous catalysts with isolated single metal atoms embedded within a solid matrix. These catalysts have attracted considerable interest in recent years due to their intriguing properties, including high metal atom utilization efficiency, controlled coordination environments of metal atoms, unique quantum size effects, and tunable metal−support interactions.[1−6] In particular, metal−nitrogen−carbon (M−N−C) SACs (where M is a metal atom coordinated with four N or C atoms within a carbon skeleton) have shown excellent catalytic activities for oxygen reduction reaction (ORR).[7−9] For example, Fe−N−C SACs are highly active for the 4e$^-$ ORR ($O_2 + 4H^+ + 4e^- \rightarrow 2H_2O$, $E^0 = 1.23$ V) in converting O_2 to H_2O,[10,11] which is an essential reaction for fuel cells and metal−air batteries.[12,13] Co−N−C SACs show a high selectivity toward the 2e$^-$ ORR ($O_2 + 2H^+ + 2e^- \rightarrow H_2O_2$, $E^0 = 0.70$ V) to produce H_2O_2,[14,15] which is an imperative chemical for many applications.[16,17]

M−N−C SACs have been synthesized by either bottom-up methods, such as atomic layer deposition, wet chemistry synthesis via binding metal ions to carbon matrixes, or ball-milling, as well as top-down methods, including pyrolysis of metal-containing complexes, metal−organic frameworks, polymers, and small organic precursors, or some solid-state reactions.[18−21] Metal atoms in M−N−C SACs resulting from these synthesis methods are often at unique coordination sites with distinct catalytic properties. Further, carbon matrixes with different doped atoms, chemical functional groups, or defects may also have high catalytic activities.[22−25] Alternatively, organometallic complexes containing M−N−C active sites have been studied as homogeneous ORR catalysts for decades.[26−29] Tetradentate N coordination sites can firmly anchor metal atoms.[30] Previous studies have assembled porphyrin- or phthalocyanine-based organometallic complexes on graphene or carbon nanotubes as M−N−C SACs.[31−33] Although metal coordination sites in these catalysts are identical, graphene or carbon nanotube substrates induce charge transfer to M−N−C active sites, which is expected to significantly alter their catalytic activities.[34] Carbon materials in these catalysts can also contribute to the observed catalytic activities. On the other hand, various theoretical descriptors have been proposed to explain the catalytic activity of M−N−C SACs, such as intermediates adsorption energies,[13,35−38] metal d-band centers,[39] and metal−crystal field stabilization energies.[40] However, because existing M−N−C SACs lack

Received: October 6, 2020
Published: December 17, 2020

https://dx.doi.org/10.1021/jacs.0c10636

well-defined and uniformly distributed metal centers without added interferences from various other catalytic active species, their precise structure−activity relationships in M−N−C SACs remain unclear.[37,41,42]

Here, we unambiguously reveal the intrinsic electrocatalytic activity of various metal centers in M−N−C SACs for H_2O_2 synthesis using two-dimensional (2D) covalent organic framework (COF)-based model catalysts (denoted as COF-366-M). The conjugated porphyrin-based COF (COF-366) is a coordination 2D polymer crystal with a periodically repeating architecture.[43] Its abundant porphyrin moieties can host a variety of 3d transition metals or noble metals with an identical chemical structure. Further, their conjugated polymer framework provides sufficient electron-transfer capability without the need to add carbon material substrates, while the 2D porous nanosheet structure enables efficient mass transfer. Our experimental studies show that Co centers have the highest activities among 3d transition metals, including Mn, Fe, Co, Ni, Cu, and Zn, in three types of electrolytes at different pH values. Using density functional theory (DFT) calculations, we show that the binding energy difference between O_2* and HOOH* intermediates ($E_{O_2*} - E_{HOOH*}$) at single metal sites can be used as a general descriptor to predict the intrinsic catalytic activity of these metal centers, including ten 3d transition metals and eight noble metals, in COF-366-M. Experimental results further corroborate the prediction of COF-366-Ir as a highly active catalyst.

2. METHODS

Chemicals and Materials. 5,10,15,20-(Tetra-4-aminophenyl) porphyrin (TAPP, 98%) was purchased from PorphyChem, Inc. Terephthaldehyde (TPD, 99%), $Mn(OAc)_2$ (99.99%), $Fe(OAc)_2$ (99.99%), $Co(OAc)_2 \cdot 4H_2O$ (99.99%), $Ni(OAc)_2 \cdot 4H_2O$ (99.99%), $Cu(OAc)_2$ (99.99%), $Zn(OAc)_2 \cdot 2H_2O$ (99.99%), $IrCl_3 \cdot H_2O$ (99.9%), Na_2SO_4 (anhydrous, >99%), KOH (99.9%, semiconductor grade), NaOAc (99%), KH_2PO_4 (99%), K_2HPO_4 (99%), $CeSO_4 \cdot 4H_2O$ (98%), methylene blue (97%), acetic acid (99.9%), KSCN (99%), methanol (anhydrous, 99.9%), ethanol (200 proof, anhydrous, >99.5%), *N*,*N*-dimethylformamide (DMF, anhydrous, 99.8%), mesitylene (98%), chloroform (>99.5%), benzonitrile (anhydrous, 99%), and H_2O_2 solution (30 wt %) were purchased from Sigma-Aldrich. Ar (5.0 grade) and O_2 (4.5 grade) gases were purchased from BOC Australia.

Synthesis of TAPP-M. In a typical synthesis, 0.3 mmol TAPP (200 mg) and 1.2 mmol metal acetate salt were suspended in 20 mL of methanol before the addition of 90 mL of chloroform and 30 mL of DMF. The mixture was stirred under Ar protection at 80 °C for 24 h. After cooling to room temperature, the solution was transferred into a separatory funnel and washed thoroughly with deionized (DI) water (18.2 MΩ, Millipore, 3 × 100 mL). The organic layer was collected and dried over anhydrous Na_2SO_4, and the product was further vacuum-dried overnight to obtain the final product. For the synthesis of TAPP-Ir, a mixture of 0.035 mmol TAPP (23 mg) and 0.14 mmol $IrCl_3 \cdot H_2O$ (50 mg) was mixed in 50 mL of benzonitrile. The mixture was refluxed for 24 h under Ar protection. Afterward, the procedure is the same as that used for other TAPP-M.

Synthesis of COF-366 and COF-366-M. They were synthesized via the imine condensation in solvothermal reactions. TAPP or TAPP-M (0.02 mmol) and 0.04 mmol TPD were suspended in a mixture of 1 mL of absolute ethanol, 1 mL of mesitylene, and 0.1 mL of 6 M acetic acid in a Pyrex tube by sonication. After sonication for 15 min, the tube was flash-frozen at 77 K (liquid N_2 bath), evacuated to an internal pressure of 150 mTorr, and then flame-sealed. After reaction at 120 °C for 72 h, the dark purple solids were collected by vacuum filtration and washed with dimethylacetamide (DMAC) and absolute ethanol before drying under vacuum.

Materials Characterization. Scanning electron microscopy (SEM) images were collected on a Zeiss Ultra Plus microscope. High-angle annular dark-field scanning transmission electron microscopy (HAADF-STEM) images were collected on an FEI Themis-Z microscope. Fourier transform infrared (FTIR) spectra were collected on a Thermo Scientific Nicolet 6700 spectrometer using the attenuated total reflection mode. X-ray diffraction (XRD) patterns were obtained on a PANalytical X'Pert diffractometer using a Cu Kα source (λ = 1.5406 Å). N_2 physisorption isotherms were collected on a Quantachrome Autosorb iQ2 gas sorption analyzer. Atomic force microscopy (AFM) height profiles were obtained on a Park NX10 microscope using the noncontact mode. The samples were acid-digested in HNO_3 for 6 h before inductively coupled plasma atomic emission spectroscopy (ICP-AES) elemental analysis on a Varian Vista Pro instrument. X-ray photoelectron spectroscopy (XPS) spectra were collected on a Thermo Fisher K-Alpha+ spectrometer equipped with an Al Kα source (1486.3 eV). X-ray absorption spectroscopy (XAS) spectra were collected in fluorescence mode on the BL-12B2 beamline at the National Synchrotron Radiation Research Center, Taiwan. The energy was tuned by a double-crystal Si (111) monochromator. Data analysis and fitting were performed with the Demeter package using the FEFF 9.0 code.

Electrochemical Measurements. Catalysts were dispersed in a 1/9 water/isopropanol (v/v) solution (with 0.05 wt %/v Nafion 117) at a concentration of 1 mg mL^{-1} by bath sonication for 30 min. The catalyst ink was then drop-casted on prepolished glassy carbon disk of rotating ring-disc electrodes (RRDEs) with a Pt ring electrode (Pine Instrument, disk o.d. of 5.5 mm, ring i.d. of 6.5 mm, and o.d. of 8.5 mm) with a mass loading of 5 μg cm^{-2}. Electrochemical measurements were conducted on a CHI 760E electrochemical workstation in a three-electrode configuration with a graphite rod (Pine) as the counter electrode and an Ag/AgCl (sat. KCl) electrode as the reference electrode at 25 °C. All potentials were subjected to a reversible hydrogen electrode (RHE) by adding 0.197 + pH × 0.059 V. Three types of O_2-saturated electrolytes were used, including 0.1 M KOH (pH = 12.6), 0.1 M phosphate-buffered saline (PBS) (pH = 7.4), and 0.1 M sodium acetate solution (ABS) (pH = 3.5). Before commencing ORR performance measurements, RRDEs were precycled with 20 cyclic voltammetry (CV) scans between 0.1 and 1 V versus RHE. Linear sweep voltammetry (LSV) polarization measurements were performed under a scan rate of 2 mV s^{-1} with a rotation speed of 1600 rpm without *iR* correction. The potential of the Pt ring was kept at 1.2 V versus RHE. The onset potentials are defined as the potential required to reach a geometric current density of −0.05 mA cm^{-2} for the disk electrode (U_{disk}) and 0.02 mA cm^{-2} for the ring electrode (U_{ring}), respectively. The influence of SCN$^-$ adsorption was assessed by collecting LSV polarization curves in O_2-saturated 0.1 M ABS with or without adding 0.1 M KSCN. ORR electron transfer number (n) is determined by the following equation,

$$n = 4 \times \frac{i_{disk}}{i_{disk} + i_{ring}/N} \tag{1}$$

where i_{disk} and i_{ring} are the currents obtained from the glassy carbon disk and Pt ring, respectively. N is the calibrated collection efficiency of RRDEs (N = 0.38). The selectivity toward H_2O_2 formation can be evaluated by two methods: Faradaic efficiency ($\lambda_{Faradaic}$, %) or the fraction of O_2 reduced to H_2O_2 ($\lambda_{H_2O_2}$, %).

$$\lambda_{Faradaic} = \frac{\frac{i_{ring}}{N}}{i_{disk}} \times 100 \tag{2}$$

$$\lambda_{H_2O_2} = \frac{2 \times i_{ring}/N}{i_{disk} + i_{ring}/N} \times 100 \tag{3}$$

The following equations were used to calculate the product-specific current density for H_2O_2 formation ($j_{H_2O_2}$) and H_2O formation (j_{H_2O}),

$$j_{H_2O_2} = i_{ring}/(N \times A_{geom}) \tag{4}$$

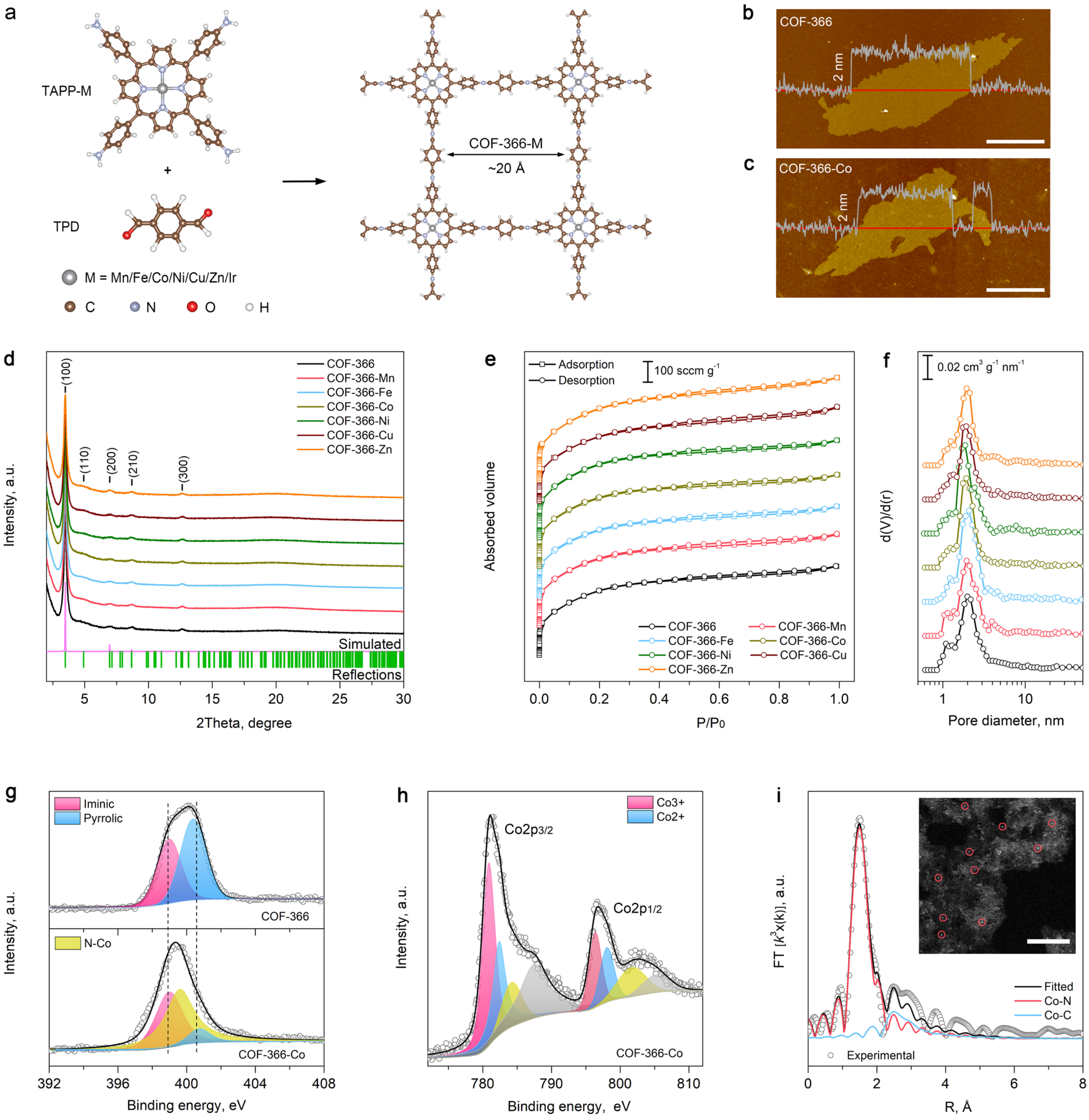

Figure 1. Synthesis and structural characterization of COF-366-M. (a) Schematic illustration of the synthesis of COF-366-M. (b, c) AFM images of COF-366 and COF-366-Co and the corresponding height profiles along the red lines; the scale bar is 500 nm. (d) XRD patterns. (e) N_2 physisorption isotherms. (f) Pore-size distribution. (g) High-resolution N1s XPS spectra. (h) High-resolution Co 2p XPS spectra. (i) Fitted Co K-edge extended X-ray absorption fine structure (EXAFS) spectrum of COF-366-Co. The inset shows a HAADF-STEM image. The scale bar is 5 nm.

$$j_{H_2O} = j_{disk} - j_{H_2O_2} \tag{5}$$

where A_{geom} is the surface area of the Pt ring.

The kinetic limiting current density j_K was extracted from the polarization curves using the K−L equation,

$$\frac{1}{j} = \frac{1}{j_L} + \frac{1}{j_K} = \frac{1}{B\omega^{1/2}} + \frac{1}{j_K} \tag{6}$$

$$B = 0.62nFC_0(D_0)^{2/3}\upsilon^{-1/6} \tag{7}$$

where j is the measured current density and j_L and j_K are the diffusion-limiting and kinetic current densities, respectively. ω is the angular velocity, n is electron transferred number, F is the Faraday constant, C_0 is the saturated concentration of O_2 in electrolytes at room temperature, D_0 is the diffusion coefficient of oxygen in the electrolytes, and υ is the kinematic viscosity of the electrolyte at 25 °C. Tafel analysis was performed by using the extracted j_K values. The mass-specific current density ($j_{K\text{-mass}}$, mA mg^{-1} cm^{-2}) and the turnover frequency (TOF) of the catalysts were calculated by using the following equations,

$$j_{\text{K-mass}} = \frac{j_{\text{K}} \times \lambda_{\text{H}_2\text{O}_2} \times A_{\text{disk}}}{0.005} \tag{8}$$

$$\text{TOF} = \frac{j_{\text{K}} \times \lambda_{\text{H}_2\text{O}_2} \times A_{\text{disk}}}{n \times m \times w \times F/M_{\text{w}}} \tag{9}$$

where 0.005 (mg cm^{-2}) is the catalyst loading. A_{disk} is the geometric surface area of the disk electrode, $n = 2$ is the electron-transfer number for H_2O_2 formation, m is the mass of the catalyst loaded on the disk electrode, w is the metal composition by weight, and M_w is the molar weight of the metal. F is the Faraday constant. H_2O_2RR tests were carried out by subtracting LSV currents measured in Ar-saturated 0.1 M ABS containing 1 mM H_2O_2 from the background LSV currents measured in Ar-saturated 0.1 M ABS without H_2O_2.

DFT Calculations. All DFT calculations were performed with the Vienna ab initio simulation package. Valence electrons were described by the Kohn−Sham wave functions expanded in a plane-wave basis set.[44] Electron correlation was described by a generalized gradient approximation method and the Perdew−Burke−Ernzerhof (PBE) functional.[45,46] Core electrons were described by a projector augmented-wave method.[47] Geometries were defined as converged when all the force on each atom fell below 0.05 eV Å^{-1}. The Brillouin zone was sampled at the Γ-point. Spin-polarization was considered in all the calculations. The kinetic barriers were calculated by the climbing image nudged elastic band (CI-NEB) method, with at least six images located between the initial and final states.[48] Entropic corrections (at a temperature of 298 K) and zero-point energies were applied in the free energy calculations, with the values taken from a previous study.[49] The binding energies of O_2 ($E_{O_2}*$) and HOOH ($E_{\text{HOOH}*}$) were calculated using

$$E_{O_2*} = E_{\text{tot}} - E_{\text{bare}} - E_{O_2} \tag{10}$$

$$E_{\text{HOOH}*} = E_{\text{tot}} - E_{\text{bare}} - E_{\text{HOOH}} \tag{11}$$

where E_{tot} is the total energy of the system with adsorbate, E_{bare} is the total energy of the bare system, E_{O_2} is the total energy of an O_2 molecule in a vacuum, and E_{HOOH} is the total energy of an H_2O_2 molecule in a vacuum. To test the sensitivity of the applied functional, similar calculations using the revised Perdew−Burke−Ernzerhof (RPBE) functional were also performed.[50] Except for a slight systematic shift in the O_2 binding energies compared to PBE (∼0.18 ± 0.13 eV), no significant change was found in the adsorption configuration.

3. RESULTS AND DISCUSSION

Synthesis and Structural Characterization of COF-366-M. We synthesized COF-366-M with an imine condensation reaction.[51] As illustrated in Figure 1a, 5,10,15,20-(tetra-4-aminophenyl) porphyrin salts loaded with different 3d-transition metal ions (TAPP-M, M = Mn, Fe, Co, Ni, Cu, and Zn) react with TPD in solvothermal reactions (see details in the Methods section). COF-366 without metals was also synthesized as a reference. New imine bond vibrations at $\nu_{C=N}$ of 1621 and 1192 cm^{-1} in FTIR confirm the successful formation of COF-366 (Figure S1). As-synthesized COF-366-M and COF-366 self-assemble into microspheres with a diameter of ∼500 nm (see SEM images in Figures S2 and S3). These microspheres can be easily delaminated into 2D nanosheets by simple bath-sonication in organic solvents (e.g., *N,N*-dimethylformamide or *N*-methyl-2-pyrrolidone). Parts b and c of Figure 1 show AFM images of delaminated COF-366 and COF-366-Co nanosheets with thicknesses of ∼2 nm. The other COF-366-M catalysts exhibit similar morphologies in their delaminated nanosheets (Figure S4). XRD patterns of COF-366-M catalysts (Figure 1d) exhibit identical peaks at 2θ of 3.47°, 6.96°, 8.66°, and 12.60°, corresponding to (100), (200), (111), and (310) facets of COF-366, respectively, consistent with a simulated eclipsed stacking model.[52] No other metal or metal oxide XRD peaks are observed. The XRD results indicate that the incorporation of 3d-metals does not affect the crystal structure of COF-366. N_2 physisorption isotherms (shifted in the y-axis) of COF-366-M and COF-366 in Figure 1e are all type I isotherms. The Brunauer−Emmett−Teller (BET) specific surface areas of COF-366-M are comparable from 998 to 1117 $\text{m}^2\ \text{g}^{-1}$ (Table S1). Figure 1f shows that they also have similar pore-size distributions calculated by the DFT method, agreeing with the porous structure shown in their physical model in Figure 1a.[52,53]

Both XPS (Figure S5) and ICP-AES confirm that the abundance of 3d metals in COF-366-M is similar at around 0.77 to 0.84 at% (Table S1). C 1s XPS spectra (Figure S6) suggest that COF-366-M have identical chemical structures in their C atoms. N 1s XPS spectra (Figure 1g and Figure S7) display that the position (at 398.4 eV) and abundance of N in imine bonds are the same in COF-366 and COF-366-M. However, pyrrolic-N in porphyrin rings (at 399.4 eV in COF-366) shifts to a higher binding energy in COF-366-Co due to the interactions between N and Co. The deconvolution of metal 2p XPS spectra (Figure 1h and Figure S8) indicates that most of the 3d transition metals incorporated into COF-366-M are in their divalent state, except that Co in COF-366-Co and Fe in COF-366-Fe are in mixed divalent and trivalent states. We also collected the electron paramagnetic resonance (EPR) of Co in COF-366-Co (Figure S9). The featureless EPR spectrum suggests that Co is at a low-spin state ($S = 0$), promoting Co-active sites' electrochemical activity.[54] Because the redox potential of $\text{Co}^{2+/3+}$ and $\text{Fe}^{2+/3+}$ is 1.25 V and 0.75 V versus RHE, respectively, both Co and Fe would be reduced to their divalent states under the applied potential used for ORR.[37,55]

We further analyzed the representative COF-366-Co by XAS. Its k^3-weighted Fourier-transformed extended X-ray absorption fine structure (FT-EXAFS) spectrum at the Co K-edge was fit over the first and second Co shells. Figure 1i shows a sharp peak at 1.54 Å originating from Co−N bonds, while the peaks from Co−C bonds in the porphyrin rings in the second shell are weak, indicating that Co atoms are isolated in the porphyrin. The catalysts were further examined by atomic-resolution STEM conducted in HAADF mode. The inset of Figure 1i and other images in Figure S10 show isolated bright spots of single metal atoms without metal aggregates. Overall, the physicochemical characterization results confirm that all COF-366-M catalysts have similar physical structures and metal abundance, and the incorporated 3d transition metals are present in the same chemical environment in the porphyrin.

Experimental Evaluation of the Catalytic Activity of COF-366-M. We evaluated the electrocatalytic performance of COF-366-M for ORR by the RRDE method (Figure S11 and the related description). Three types of O_2-saturated electrolytes at different pH values were used, including alkaline 0.1 M KOH (pH = 12.6), neutral 0.1 M PBS (pH = 7.2), and acidic 0.1 M ABS (pH = 3.5) electrolytes. Catalysts were drop-cast on a prepolished and calibrated glassy carbon disk electrode that has a collection efficiency of 0.38 (Figure S12).[56] The catalyst mass loading on the disk electrodes was also optimized; 5 μg cm^{-2} was used in this study (Figure S13 and the related discussion). Figure 2a and Figure S14 show

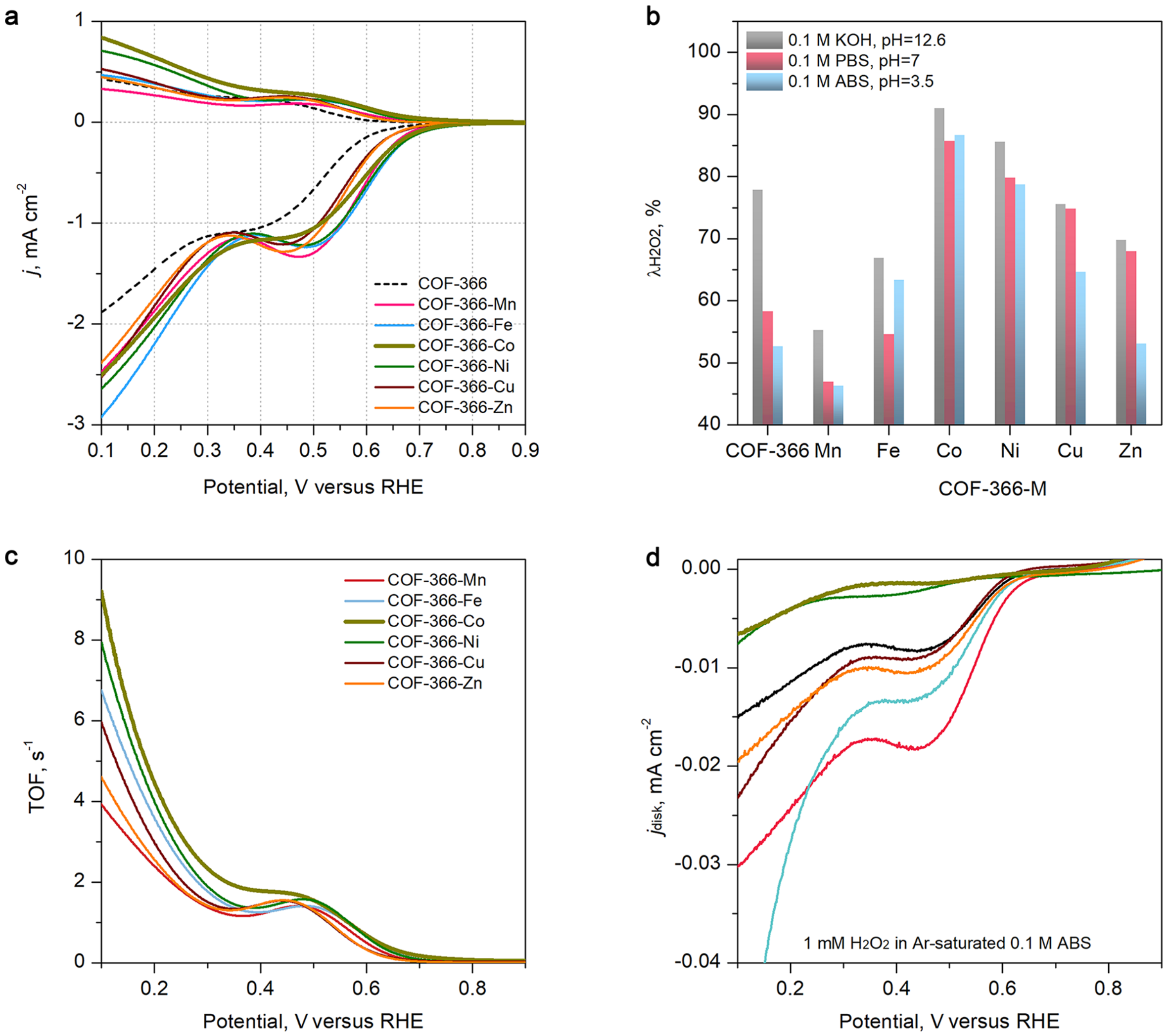

Figure 2. Electrocatalytic performance of COF-366-M. (a) ORR RRDE polarization curves of COF-366 and COF-366-M in O_2-saturated 0.1 M KOH (pH = 12.6). (b) H_2O_2 selectivity in three types of electrolytes. (c) TOF of COF-366-M catalysts. (d) Catalytic activity of COF-366-M catalysts for the H_2O_2RR.

polarization LSV curves of COF-366-M collected from the disk and ring electrodes in the three types of O_2-saturated electrolytes. All tested COF-366-M catalysts exhibit higher disk current densities (j_{disk}) and more positive disk onset potentials (U_{disk}) than COF-366, indicating that the metal atoms in COF-366-M are active catalytic sites. As tabulated in Table S2, COF-366-Fe has the highest activity for ORR, delivering the largest j_{disk} of 2.90 mA cm^{-2} at 0.1 V versus RHE and the most positive U_{disk} at 0.803 V versus RHE. The overall trend for the ORR activity is COF-366-Fe > Ni > Mn ≈ Co > Cu > Zn.

The i_{ring} in the upper panel in Figure 2a and Figure S14 were compared to evaluate the selectivity toward H_2O_2 formation. Results tabulated in Table S2 show that COF-366-Co delivers the highest i_{ring} of 0.199 mA at 0.1 V versus RHE in 0.1 M KOH, followed by COF-366-Ni at 0.168 mA. The overall selectivity trend toward H_2O_2 formation is COF-366-Co > Ni > Cu > Fe > Zn > Mn in 0.1 M KOH. Similar patterns were observed in both neutral and acidic electrolytes. We further compared the selectivity toward H_2O_2 of COF-366-M catalysts quantitatively, based on $\lambda_{H_2O_2}$ and the electron-transfer number (n, Figure S15). The values of $\lambda_{H_2O_2}$ at 0.3 V versus RHE of different COF-366-M catalysts, as displayed in Figure 2b, exhibit a volcano-shaped curve. As summarized in Table S3, COF-366-Co has the highest $\lambda_{H_2O_2}$ of 91% and $\lambda_{\mathrm{Faradaic}}$ of 84% in 0.1 M KOH electrolyte, exhibiting a high selectivity toward H_2O_2 formation by the 2e$^-$ transferred ORR. In comparison, COF-366-Mn is more selective toward 4e$^-$ ORR to produce H_2O. We further extracted j_K of different catalysts and calculated the mass-specific H_2O_2 current density ($j_{\mathrm{K\text{-}mass}}$, Figure S16). COF-366-Co can deliver a $j_{\mathrm{K\text{-}mass}}$ of nearly 977 mA cm^{-2} mg^{-1} at 0.2 V versus RHE. Figure 2c shows the H_2O_2 production turnover frequency (TOF) of the metal centers in COF-366-M. COF-366-Co delivers a superior TOF of 1.79 s^{-1} at 0.4 V versus RHE, which is ~1.3 times higher than COF-366-Ni at 1.37 s^{-1}. COF-366-Co maintains a high H_2O_2 selectivity in a wide potential window, and its TOF reaches 9.05 s^{-1} at 0.1 V versus RHE. The Tafel slopes of COF-366-M catalysts in the three electrolytes were calculated from their j_K. Figure S17 and Table S4 revealed similar Tafel slopes, suggesting that they have the same rate-limiting step in the different electrolytes.[57]

We further evaluated the H_2O_2 production capability of the optimal COF-366-Co catalyst in an H-shaped electrolyzer

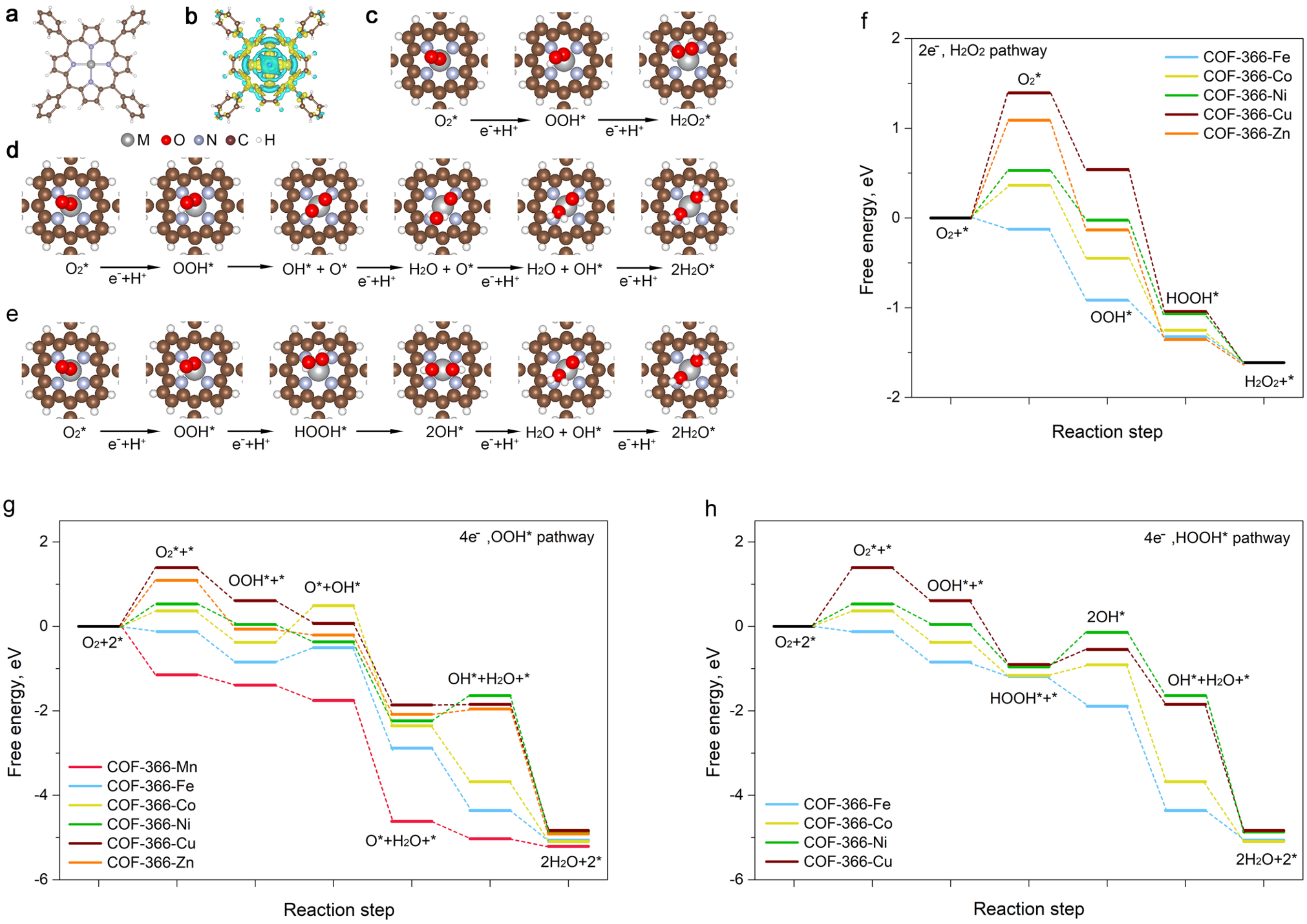

Figure 3. DFT calculation results of ORR on COF-366-M. (a) Optimized geometry of COF-366-Co. (b) Charge density difference before and after incorporating Co in the porphyrin moiety. (c−h) Geometries of adsorbed reaction intermediates and adsorption energies on COF-366-Co at $U = 0$ V. (c, f) ORR via the 2e$^-$ pathway toward H_2O_2 formation, (d, g) ORR via the OOH dissociation 4e$^-$ pathway, and (e, h) ORR via the HOOH dissociation 4e$^-$ pathway.

(Figure S18). The electrolyzer can operate steadily in ambient air, delivering a gradually increasing H_2O_2 productivity (Figure S19a) as quantified by a $Ce(SO_4)_2$ titration method (Figure S20). The COF-366-Co catalyst can produce H_2O_2 up to 909 mmol g_{cat}^{-1} h^{-1} at a current density of 22 mA cm^{-2} with a device Faradaic efficiency (λ_{device}) of 79%. The catalyst stability was evaluated by a 3 h chronopotentiometric test performed at 22 mA cm^{-2} (Figure S19b). The operating potential remained stable, while the cumulative H_2O_2 concentration ($c_{H_2O_2}$) increased linearly. Negligible morphological changes were observed under HADDF-STEM and Co 2p XPS spectrum after the stability test (Figure S21). The $c_{H_2O_2}$ reached 337 mM after the 3-h test, which is sufficient to be utilized directly for wastewater remediation via Fenton reaction. As a demonstration, we added 5 mL of the catholyte into 10 mL of acidified methylene blue solution (200 mg L^{-1}, pH = 1, with 0.1 mmol Fe^{2+}, Figure S22a). After a brief hand-shaking, the color of the solution quickly faded (Figure S22b). UV−vis absorption measurements further confirmed the complete removal of the dye (Figure S22c).

H_2O_2 produced from ORR may be further reduced to water via the H_2O_2 reduction reaction (H_2O_2RR) by the same catalyst, which would sabotage H_2O_2 production. We compared the catalytic activity of COF-366-M for H_2O_2RR, and their polarization curves were collected in an Ar-saturated 0.1 M ABS electrolyte containing 1 mM H_2O_2. The background-corrected j_{disk} in Figure 2d indicates that the activity for H_2O_2RR agrees with the selectivity toward H_2O_2 obtained in the ORR tests discussed earlier. COF-366-Co is almost inert to H_2O_2RR with a negligible measured j_{disk}. In contrast, COF-366-Fe and COF-366-Mn are highly active for H_2O_2RR. They also tend to adsorb H_2O_2 molecules and further break the O−O bonds to produce H_2O.

Theoretical Insights on the Catalytic Activity of COF-366-M. DFT calculations were used to understand the catalytic activity of metal centers in COF-366-M. Figure 3a shows the optimized geometry of COF-366-Co. Figure 3b displays the calculated charge density difference before and after incorporating a Co atom into the porphyrin ring, which indicates a significant charge redistribution with an electron delocalized from the metal center to the conjugated 2D COF. The direct O_2 dissociation is less favorable on the metal site because two O* (* stands for the active site) cannot be stably coadsorbed. The free energy of the reaction intermediates on COF-366-M was calculated by the computational hydrogen electrode method.[49] Figure 3c illustrates the ORR along the 2e$^-$ transferred pathway on COF-366-M. ORR may also proceed via the 4e$^-$ transferred pathways by either OOH dissociation (Figure 3d) or H_2O_2 dissociation (Figure 3e). The

https://dx.doi.org/10.1021/jacs.0c10636
J. Am. Chem. Soc. 2020, 142, 21861−21871

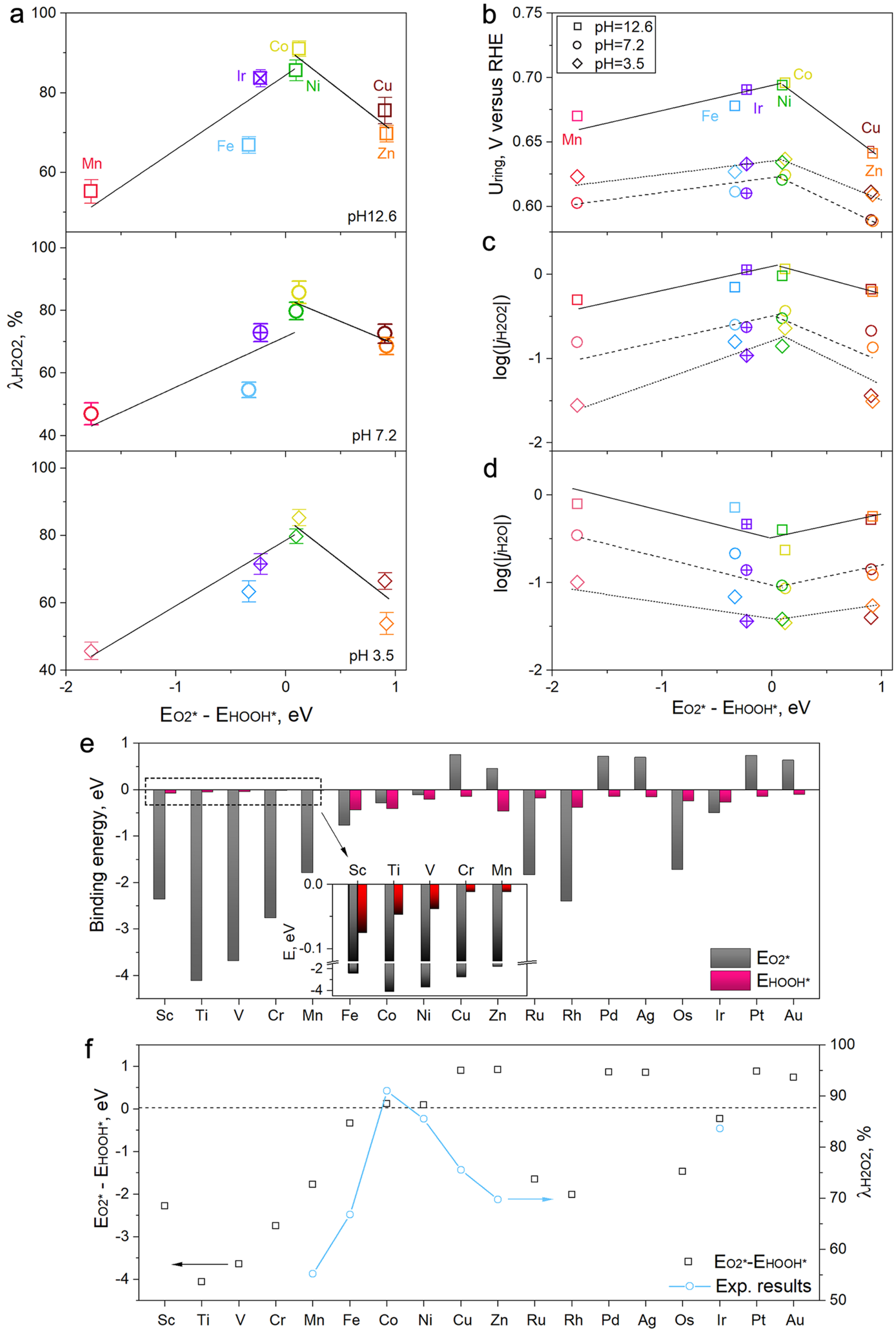

Figure 4. Validation of the thermodynamic descriptor ($E_{O_2*} - E_{HOOH*}$) on COF-366-M catalysts. (a) Correlation between $E_{O_2*} - E_{HOOH*}$ and ORR performance parameter, O_2 efficiency ($\lambda_{H_2O_2}$), in the three electrolytes. Correlation between $E_{O_2*} - E_{HOOH*}$ and (b) onset potential for ring electrode (U_{ring}), (c) specific current density for H_2O_2 formation ($j_{H_2O_2}$) at 0.3 V versus RHE, and (d) specific current density for H_2O formation (j_{H_2O}) at 0.3 V versus RHE. (e) Calculated E_{O_2*} and E_{HOOH*} on different metal centers in COF-366-M. (f) Comparison between $E_{O_2*} - E_{HOOH*}$ and experimentally measured $\lambda_{H_2O_2}$ for various COF-366-M catalysts.

corresponding free energies of reaction intermediates via the three ORR pathways are listed in Table S5 and also illustrated in parts f, g, and h of Figure 3, respectively. HOOH* is unstable on COF-366-Mn, prohibiting the formation of H_2O_2, which agrees with its lowest H_2O_2 selectivity observed in our experiments. Hence, COF-366-Mn was excluded from the calculations along the $2e^-$ transferred pathway (Figure 3f) and the H_2O_2 dissociation pathway (Figure 3h). Further, the adsorption of two OH* on COF-366-Zn is also not stable, and thus it was also excluded from the H_2O_2 dissociation pathway (Figure 3h). We further analyzed the kinetics of OOH* dissociation by the Cl-NEB method (Figure S23). We found that all of these systems have relatively large OOH* dissociation barriers (Table S6); in good agreement with our experimental results, $4e^-$ ORR is less facile at these COF-336-M. Meanwhile, because HOOH* dissociation on most of the COF-336-M is endothermic (Figure 3h), it is expected that this step also has relatively large kinetic barriers, which in turn leads to difficulty in the following $4e^-$ ORR step. Although the scaling rule between the free energies of OOH* and OH* has been widely used to explain the reaction mechanism of ORR on closely packed metal surfaces,[17,49,58] we did not observe the same scaling relation on COF-366-M. Figure 3 suggests that the $2e^-$ pathway toward H_2O_2 formation is favored over the $4e^-$ ORR pathways on COF-366-M, which agrees with the experimental observation that $\lambda_{H_2O_2}$ is >50% on all COF-366-M catalysts (Table S3).

Our DFT calculations and experimental results indicate that the selectivity of ORR toward H_2O_2 formation on COF-366-M is predominately determined by the binding strength of O_2 and HOOH intermediates on the metal sites. First, Figure 3 suggests that the adsorption of an oxygen molecule to form O_2* on metal atom sites could be the key step of H_2O_2 formation. Our calculation results (Table S5) show that O_2 adsorption on Cu or Zn is relatively weak, while it is strong enough on Co, Ni, and Fe. The effect of O_2 adsorption was experimentally validated by comparing LSV polarization curves in the ABS electrolyte with and without 0.1 M SCN^-. SCN^- can strongly bind to single metal atom sites, which would block that metal site for O_2 adsorption.[59] Figure S24 shows that the onset potential for ORR (U_{disk}) increases significantly on all COF-366-M with the addition of SCN^- in the electrolyte. We can establish an explicit correlation between the change in the onset potential (ΔU_{disk}) and the binding energy of O_2* (E_{O_2*}) on COF-366-M catalysts (Figure S25 and Table S7). Second, although O_2 adsorption on COF-366-Fe has the lowest adsorption energy, COF-366-Fe is favorable for HOOH* decomposition rather than HOOH* desorption (Figure 3h). Experimental results in Figure 2d also show that COF-366-Fe has one of the highest j_{disk} values for H_2O_2RR, which suggests that the binding strength of HOOH on the metal site is also critical for H_2O_2 formation. Overall, the optimal COF-366-M catalyst should bind to these two intermediates, neither too strongly nor too weakly.

A New Thermodynamic Descriptor to Predict Catalytic Activity. On the basis of these findings, we propose that the difference between the binding energies of O_2* and HOOH* ($E_{O_2*} - E_{HOOH*}$) may be used as a thermodynamic descriptor to describe the catalytic activity of COF-366-M catalysts for H_2O_2 formation. An intermediate E_{O_2*} is needed to promote the initial adsorption of oxygen molecules and meanwhile inhibit the activation of the O−O bond. E_{HOOH*} is related to the formation and subsequent desorption of the HOOH* reaction intermediate. As we can see from the calculated E_{HOOH*} on different systems, most of them have a moderate binding to the metal center with the absolute HOOH binding energies slightly below zero. Therefore, an ideal center metal at COF-366 is expected to have moderate binding energies for both O2* and HOOH*.

Parts a−d of Figure 4 show correlations between the $E_{O_2*} - E_{HOOH*}$ descriptor and four experimental performance parameters in the three different electrolytes, including the H_2O_2 efficiency ($\lambda_{H_2O_2}$), the onset potential for ring electrode (U_{ring}), the specific current density for H_2O_2 formation ($j_{H_2O_2}$), and the specific current density for H_2O formation (j_{H_2O}), both obtained at 0.3 V versus RHE. Each of these correlations shows a volcano-shaped curve for the different COF-366-M catalysts. COF-366-Co and COF-366-Ni sit on the top of the curves of the catalytic performance parameters, while their $E_{O_2*} - E_{HOOH*}$ approaches zero. Therefore, we can set a clear target ($E_{O_2*} - E_{HOOH*} \approx 0$ eV) to rapidly screen promising COF-366-M catalysts according to this empirical descriptor. Note that this new descriptor is the electronic energy; the use of free energy would lead to the same conclusion since the entropic terms among the different SAC systems are similar. We also plotted $\lambda_{H_2O_2}$ against several commonly used thermodynamic descriptors (Figure S26)[60] and E_{O_2*} or E_{HOOH*} alone (Figure S27); none of the other descriptors show a better correlation with our experimental data.

The close agreement between our experimental and theoretical results suggests that the volcano-like trend for selective H_2O_2 formation among the tested COF-366-M catalysts may be used with the $E_{O_2*} - E_{HOOH*}$ descriptor to predict the catalytic performance of other transition metals in a similar molecular structure, i.e., $M-N_4/C$ in porphyrin-like molecules. We computed E_{HOOH*} and E_{O_2*} on single-atom sites in 12 other COF-366-M catalysts, in which M includes four other early 3d transition metals (Sc, Ti, V, and Cr) and eight different noble metals (Ru, Rh, Pd, Ag, Os, Ir, Pt, and Au). The results are displayed in Figure 4e and Table S8. E_{O_2*} on the early 3d transition metals is much stronger (i.e., more negative) than E_{HOOH*}, suggesting that the O−O bond cannot be easily retained at these sites, resulting in unfavorable conditions for H_2O_2 formation. The revised Perdew−Burke−Ernzerhof (RPBE) functional was also used to test the sensitivity of the applied functional. Table S8 shows that, except for a slight systematic shift in the O_2 binding energies compared to PBE (∼0.18 ± 0.13 eV), no significant change was found in the adsorption configuration.

We overlapped the $E_{O_2*} - E_{HOOH*}$ descriptor on the experimental results in Figure 4f to show that COF-366-M incorporated with early 3d metal centers are not predicted to be active for H_2O_2 formation. There is no clear trend among COF-366-M incorporated with noble metals. Ir stands out among the noble metals considered with a near-zero binding energy difference between O_2* and HOOH*, suggesting that COF-366-Ir may be selective for H_2O_2 synthesis. On the basis of this theoretical prediction, we synthesized a COF-366-Ir catalyst (details are provided in the Methods section). AFM measurements (Figure S28) suggested that the COF-366-Ir exhibits an identical nanosheet morphology to other COF-366-

M samples. The formation of single-atom Ir sites was confirmed by HAADF-STEM, XPS, and EXAFS analyses (Figure S29). The Ir abundance in COF-366-Ir was determined by ICP-AES at 0.81 at%, similar to other COF-366-M. The catalytic performance of COF-366-Ir was evaluated, and the results are shown in Figure S30. COF-366-Ir exhibits $\lambda_{H_2O_2}$ of 83% and $\lambda_{Faradaic}$ of 71% in a 0.1 M KOH electrolyte, which fits well with the experimentally measured catalytic activity trend observed for other COF-366-M catalysts incorporated with 3d transition metals (Figure 4f).

4. CONCLUSIONS

In summary, we synthesized a series of 2D COF-based M−N−C SACs, in which different metals can be incorporated at porphyrin moieties with the same structure and catalytic active site density. These COF-366-M catalysts allowed us to compare and understand the catalytic activity and selectivity of different metal centers for H_2O_2 synthesis via ORR in alkaline, neutral, and acidic electrolytes. COF-366-Co is the most active with a high $\lambda_{H_2O_2}$ at 91%, $\lambda_{Faradaic}$ at 84%, a large TOF of 9.05 s^{-1} per Co site, and productivity of 909 mmol g_{cat}^{-1} h^{-1}, which is one of best among recently reported catalysts (Table S9). Combing experimental and computational approaches, we show that the initial O_2 adsorption and the stability of HOOH* intermediate govern the activity and selectivity toward H_2O_2 formation collaboratively. The binding energy difference between the O_2* and HOOH* intermediate ($E_{HOOH*} - E_{O_2*}$) can be used as a thermodynamic descriptor to evaluate the catalytic performance of different metal centers in COF-366-M, including both 3d transition metals and noble metals. Other than Co and Ni, Ir was predicted to have a high catalytic performance, which was subsequently verified experimentally. These findings shed new light on the rational design of M−N−C SACs of precisely controlled structures for ORR and beyond. The thermodynamic descriptor established here may be extendable to other ORR catalysts with well-defined structures.

■ ASSOCIATED CONTENT

Supporting Information

The Supporting Information is available free of charge at https://pubs.acs.org/doi/10.1021/jacs.0c10636.

> Additional experimental results including FTIR spectra, SEM images of COF-366 and COF-366-M, additional AFM images of COF-366-M, XPS survey scans, C 1s, N 1s, and M2p spectra, HAADF-STEM images of COF-366-M, RRDE calibration curves, catalyst mass loading optimization, ORR performance, TOF values and Tafel curves of COF-366-M in electrolytes of different pH values, ORR electrolyzer diagram and H_2O_2 production performance, dye removal, poststability test STEM and XPS results, SCN^- poisoning test, correlations between experimental performance and theoretical descriptors, and characterization results and ORR performance of COF-366-Ir; and tabulated structural characterization results and detailed computation data (PDF)

■ AUTHOR INFORMATION

Corresponding Authors

Graeme Henkelman − *Department of Chemistry and the Oden Institute for Computational and Engineering Sciences, The University of Texas at Austin, Austin, Texas 78712, United States;* orcid.org/0000-0002-0336-7153; Email: henkelman@utexas.edu

Li Wei − *School of Chemical and Biomolecular Engineering, The University of Sydney, Darlington, New South Wales 2006, Australia;* orcid.org/0000-0001-8771-2921; Email: l.wei@sydney.edu.au

Yuan Chen − *School of Chemical and Biomolecular Engineering, The University of Sydney, Darlington, New South Wales 2006, Australia;* orcid.org/0000-0001-9059-3839; Email: yuan.chen@sydney.edu.au

Authors

Chang Liu − *School of Chemical and Biomolecular Engineering, The University of Sydney, Darlington, New South Wales 2006, Australia*

Hao Li − *Department of Chemistry and the Oden Institute for Computational and Engineering Sciences, The University of Texas at Austin, Austin, Texas 78712, United States;* orcid.org/0000-0002-7577-1366

Fei Liu − *State Key Laboratory of Applied Microbiology Southern China, Guangdong Provincial Key Laboratory of Microbial Culture Collection and Application, Guangdong Institute of Microbiology, Guangdong 510070, P. R. China*

Junsheng Chen − *School of Chemical and Biomolecular Engineering, The University of Sydney, Darlington, New South Wales 2006, Australia*

Zixun Yu − *School of Chemical and Biomolecular Engineering, The University of Sydney, Darlington, New South Wales 2006, Australia*

Ziwen Yuan − *School of Chemical and Biomolecular Engineering, The University of Sydney, Darlington, New South Wales 2006, Australia;* orcid.org/0000-0002-3331-0668

Chaojun Wang − *School of Chemical and Biomolecular Engineering, The University of Sydney, Darlington, New South Wales 2006, Australia*

Huiling Zheng − *Department of Chemistry and the Oden Institute for Computational and Engineering Sciences, The University of Texas at Austin, Austin, Texas 78712, United States;* orcid.org/0000-0001-8347-3724

Complete contact information is available at: https://pubs.acs.org/10.1021/jacs.0c10636

Author Contributions

‖C.L., H.L., and F.L. contributed equally.

Notes

The authors declare no competing financial interest.

■ ACKNOWLEDGMENTS

This work is supported by the Australian Research Council under the Future Fellowships scheme (FT160100107). Calculations at UT were supported by the Welch Foundation (F-1841) and the Texas Advanced Computing Center.

■ REFERENCES

(1) Yang, X. F.; Wang, A. Q.; Qiao, B. T.; Li, J.; Liu, J. Y.; Zhang, T. Single-atom catalysts: a new frontier in heterogeneous catalysis. *Acc. Chem. Res.* **2013**, *46* (8), 1740−1748.

(2) Zhu, C. Z.; Fu, S. F.; Shi, Q. R.; Du, D.; Lin, Y. H. Single-atom electrocatalysts. *Angew. Chem., Int. Ed.* **2017**, *56* (45), 13944−13960.

(3) Wang, A. Q.; Li, J.; Zhang, T. Heterogeneous single-atom catalysis. *Nat. Rev. Chem.* **2018**, *2* (6), 65−81.

(4) Liu, L. C.; Corma, A. Metal catalysts for heterogeneous catalysis: from single atoms to nanoclusters and nanoparticles. *Chem. Rev.* **2018**, *118* (10), 4981−5079.

(5) Jiao, L.; Jiang, H. L. Metal-organic-framework-based single-atom catalysts for energy applications. *Chem.* **2019**, *5* (4), 786−804.

(6) Gawande, M. B.; Fornasiero, P.; Zboril, R. Carbon-based single-atom catalysts for advanced applications. *ACS Catal.* **2020**, *10* (3), 2231−2259.

(7) Wang, Y.; Mao, J.; Meng, X.; Yu, L.; Deng, D.; Bao, X. Catalysis with two-dimensional materials confining single atoms: concept, design, and applications. *Chem. Rev.* **2019**, *119* (3), 1806−1854.

(8) Lu, B. Z.; Liu, Q. M.; Chen, S. W. Electrocatalysis of single-atom sites: impacts of atomic coordination. *ACS Catal.* **2020**, *10* (14), 7584−7618.

(9) Shi, Z. S.; Yang, W. Q.; Gu, Y. T.; Liao, T.; Sun, Z. Q. Metal-nitrogen-doped carbon materials as highly efficient catalysts: progress and rational design. *Adv. Sci.* **2020**, *7* (15), 2001069.

(10) Lefèvre, M.; Proietti, E.; Jaouen, F.; Dodelet, J.-P. Iron-based catalysts with improved oxygen reduction activity in polymer electrolyte fuel cells. *Science* **2009**, *324* (5923), 71.

(11) Wu, G.; More, K. L.; Johnston, C. M.; Zelenay, P. High-performance electrocatalysts for oxygen reduction derived from polyaniline, iron, and cobalt. *Science* **2011**, *332* (6028), 443−447.

(12) Shao, M. H.; Chang, Q. W.; Dodelet, J. P.; Chenitz, R. Recent advances in electrocatalysts for oxygen reduction reaction. *Chem. Rev.* **2016**, *116* (6), 3594−3657.

(13) Kulkarni, A.; Siahrostami, S.; Patel, A.; Norskov, J. K. Understanding catalytic activity trends in the oxygen reduction reaction. *Chem. Rev.* **2018**, *118* (5), 2302−2312.

(14) Xu, H.; Cheng, D.; Cao, D.; Zeng, X. C. A universal principle for a rational design of single-atom electrocatalysts. *Nat. Catal.* **2018**, *1* (5), 339−348.

(15) Gao, J.; Yang, H. b.; Huang, X.; Hung, S.-F.; Cai, W.; Jia, C.; Miao, S.; Chen, H. M.; Yang, X.; Huang, Y.; Zhang, T.; Liu, B. Enabling Direct H_2O_2 Production in Acidic Media through Rational Design of Transition Metal Single Atom Catalyst. *Chem.* **2020**, *6* (3), 658−674.

(16) Campos-Martin, J. M.; Blanco-Brieva, G.; Fierro, J. L. Hydrogen Peroxide Synthesis: An Outlook Beyond the Anthraquinone Process. *Angew. Chem., Int. Ed.* **2006**, *45* (42), 6962−84.

(17) Siahrostami, S.; Verdaguer-Casadevall, A.; Karamad, M.; Deiana, D.; Malacrida, P.; Wickman, B.; Escudero-Escribano, M.; Paoli, E. A.; Frydendal, R.; Hansen, T. W.; Chorkendorff, I.; Stephens, I. E.; Rossmeisl, J. Enabling Direct H_2O_2 Production through Rational Electrocatalyst Design. *Nat. Mater.* **2013**, *12* (12), 1137−43.

(18) Peng, Y.; Lu, B.; Chen, S. Carbon-supported single atom catalysts for electrochemical energy conversion and storage. *Adv. Mater.* **2018**, *30* (48), 1801995.

(19) Fei, H.; Dong, J.; Feng, Y.; Allen, C. S.; Wan, C.; Volosskiy, B.; Li, M.; Zhao, Z.; Wang, Y.; Sun, H.; An, P.; Chen, W.; Guo, Z.; Lee, C.; Chen, D.; Shakir, I.; Liu, M.; Hu, T.; Li, Y.; Kirkland, A. I.; Duan, X.; Huang, Y. General synthesis and definitive structural identification of MN_4C_4 single-atom catalysts with tunable electrocatalytic activities. *Nat. Catal.* **2018**, *1* (1), 63−72.

(20) Jiang, K.; Back, S.; Akey, A. J.; Xia, C.; Hu, Y.; Liang, W.; Schaak, D.; Stavitski, E.; Nørskov, J. K.; Siahrostami, S.; Wang, H. Highly selective oxygen reduction to hydrogen peroxide on transition metal single atom coordination. *Nat. Commun.* **2019**, *10* (1), 3997.

(21) Yang, Y.; Yang, Y.; Pei, Z.; Wu, K.-H.; Tan, C.; Wang, H.; Wei, L.; Mahmood, A.; Yan, C.; Dong, J.; Zhao, S.; Chen, Y. Recent progress of carbon-supported single-atom catalysts for energy conversion and storage. *Matter* **2020**, *3*, 1442−1476.

(22) Liu, X.; Dai, L. M. Carbon-based metal-free catalysts. *Nat. Rev. Mater.* **2016**, *1*, 16082.

(23) Kim, H. W.; Ross, M. B.; Kornienko, N.; Zhang, L.; Guo, J.; Yang, P.; McCloskey, B. D. Efficient hydrogen peroxide generation using reduced graphene oxide-based oxygen reduction electrocatalysts. *Nat. Catal.* **2018**, *1* (4), 282−290.

(24) Lu, Z.; Chen, G.; Siahrostami, S.; Chen, Z.; Liu, K.; Xie, J.; Liao, L.; Wu, T.; Lin, D.; Liu, Y.; Jaramillo, T. F.; Nørskov, J. K.; Cui, Y. High-efficiency oxygen reduction to hydrogen peroxide catalysed by oxidized carbon materials. *Nat. Catal.* **2018**, *1* (2), 156−162.

(25) Yan, X. C.; Jia, Y.; Yao, X. D. Defects on carbons for electrocatalytic oxygen reduction. *Chem. Soc. Rev.* **2018**, *47* (20), 7628−7658.

(26) Alt, H.; Binder, H.; Sandstede, G. Mechanism of the electrocatalytic reduction of oxygen on metal chelates. *J. Catal.* **1973**, *28* (1), 8−19.

(27) Zagal, J. H. Metallophthalocyanines as catalysts in electrochemical reactions. *Coord. Chem. Rev.* **1992**, *119*, 89−136.

(28) Collman, J. P.; Devaraj, N. K.; Decréau, R. A.; Yang, Y.; Yan, Y.-L.; Ebina, W.; Eberspacher, T. A.; Chidsey, C. E. D. A cytochrome c oxidase model catalyzes oxygen to water reduction under rate-limiting electron flux. *Science* **2007**, *315* (5818), 1565.

(29) Singh, K.; Razmjooei, F.; Yu, J.-S. Active sites and factors influencing them for efficient oxygen reduction reaction in metal-N coordinated pyrolyzed and non-pyrolyzed catalysts: a review. *J. Mater. Chem. A* **2017**, *5* (38), 20095−20119.

(30) Auwärter, W.; Écija, D.; Klappenberger, F.; Barth, J. V. Porphyrins at interfaces. *Nat. Chem.* **2015**, *7* (2), 105−120.

(31) Li, B.-Q.; Zhang, S.-Y.; Wang, B.; Xia, Z.-J.; Tang, C.; Zhang, Q. A porphyrin covalent organic framework cathode for flexible Zn-air batteries. *Energy Environ. Sci.* **2018**, *11* (7), 1723−1729.

(32) Peng, P.; Shi, L.; Huo, F.; Mi, C.; Wu, X.; Zhang, S.; Xiang, Z. A pyrolysis-free path toward superiorly catalytic nitrogen-coordinated single atom. *Sci. Adv.* **2019**, *5* (8), No. eaaw2322.

(33) Li, B.-Q.; Zhang, S.-Y.; Chen, X.; Chen, C.-Y.; Xia, Z.-J.; Zhang, Q. One-pot synthesis of framework porphyrin materials and their applications in bifunctional oxygen electrocatalysis. *Adv. Funct. Mater.* **2019**, *29* (29), 1901301.

(34) Strauss, V.; Roth, A.; Sekita, M.; Guldi, D. M. Efficient energy-conversion materials for the future: understanding and tailoring charge-transfer processes in carbon nanostructures. *Chem.* **2016**, *1* (4), 531−556.

(35) Greeley, J.; Stephens, I. E. L.; Bondarenko, A. S.; Johansson, T. P.; Hansen, H. A.; Jaramillo, T. F.; Rossmeisl, J.; Chorkendorff, I.; Norskov, J. K. Alloys of platinum and early transition metals as oxygen reduction electrocatalysts. *Nat. Chem.* **2009**, *1* (7), 552−556.

(36) Zagal, J. H.; Koper, M. T. M. Reactivity descriptors for the activity of molecular MN_4 catalysts for the oxygen reduction reaction. *Angew. Chem., Int. Ed.* **2016**, *55* (47), 14510−14521.

(37) Sun, Y.; Silvioli, L.; Sahraie, N. R.; Ju, W.; Li, J.; Zitolo, A.; Li, S.; Bagger, A.; Arnarson, L.; Wang, X.; Moeller, T.; Bernsmeier, D.; Rossmeisl, J.; Jaouen, F.; Strasser, P. Activity-selectivity trends in the electrochemical production of hydrogen peroxide over single-site metal-nitrogen-carbon catalysts. *J. Am. Chem. Soc.* **2019**, *141* (31), 12372−12381.

(38) Primbs, M.; Sun, Y.; Roy, A.; Malko, D.; Mehmood, A.; Sougrati, M.-T.; Blanchard, P.-Y.; Granozzi, G.; Kosmala, T.; Daniel, G.; Atanassov, P.; Sharman, J.; Durante, C.; Kucernak, A.; Jones, D. J.; Jaouen, F.; Strasser, P. Establishing reactivity descriptors for platinum group metal (PGM)-free Fe-N-C catalysts for PEM fuel cells. *Energy Environ. Sci.* **2020**, *13* (8), 2480−2500.

(39) Grimaud, A.; Diaz-Morales, O.; Han, B.; Hong, W. T.; Lee, Y.-L.; Giordano, L.; Stoerzinger, K. A.; Koper, M. T. M.; Shao-Horn, Y. Activating lattice oxygen redox reactions in metal oxides to catalyse oxygen evolution. *Nat. Chem.* **2017**, *9*, 457−465.

(40) Lin, C.-Y.; Zhang, L.; Zhao, Z.; Xia, Z. Design principles for covalent organic frameworks as efficient electrocatalysts in clean energy conversion and green oxidizer production. *Adv. Mater.* **2017**, *29* (17), 1606635.

(41) He, Y. H.; Hwang, S.; Cullen, D. A.; Uddin, M. A.; Langhorst, L.; Li, B. Y.; Karakalos, S.; Kropf, A. J.; Wegener, E. C.; Sokolowski, J.; Chen, M. J.; Myers, D.; Su, D.; More, K. L.; Wang, G. F.; Litster, S.; Wu, G. Highly active atomically dispersed CoN_4 fuel cell cathode catalysts derived from surfactant-assisted MOFs: carbon-shell confinement strategy. *Energy Environ. Sci.* **2019**, *12* (1), 250−260.

(42) Li, F.; Bu, Y.; Han, G.-F.; Noh, H.-J.; Kim, S.-J.; Ahmad, I.; Lu, Y.; Zhang, P.; Jeong, H. Y.; Fu, Z.; et al. Identifying the structure of Zn-N_2 active sites and structural activation. *Nat. Commun.* **2019**, *10* (1), 2623.

(43) Ding, S.-Y.; Wang, W. J. C. S. R. Covalent organic frameworks (COFs): from design to applications. *Chem. Soc. Rev.* **2013**, *42* (2), 548−568.

(44) Kohn, W.; Sham, L. J. Self-Consistent Equations Including Exchange and Correlation Effects. *Phys. Rev.* **1965**, *140* (4A), A1133−A1138.

(45) Perdew, J. P.; Burke, K.; Ernzerhof, M. Generalized Gradient Approximation Made Simple. *Phys. Rev. Lett.* **1996**, *77* (18), 3865−3868.

(46) Kresse, G.; Furthmüller, J. Efficient iterative schemes for ab initio total-energy calculations using a plane-wave basis set. *Phys. Rev. B: Condens. Matter Mater. Phys.* **1996**, *54* (16), 11169−11186.

(47) Blöchl, P. E. Projector augmented-wave method. *Phys. Rev. B: Condens. Matter Mater. Phys.* **1994**, *50* (24), 17953−17979.

(48) Henkelman, G.; Uberuaga, B. P.; Jónsson, H. A climbing image nudged elastic band method for finding saddle points and minimum energy paths. *J. Chem. Phys.* **2000**, *113* (22), 9901−9904.

(49) Nørskov, J. K.; Rossmeisl, J.; Logadottir, A.; Lindqvist, L.; Kitchin, J. R.; Bligaard, T.; Jónsson, H. Origin of the Overpotential for Oxygen Reduction at a Fuel-Cell Cathode. *J. Phys. Chem. B* **2004**, *108* (46), 17886−17892.

(50) Hammer, B.; Hansen, L. B.; Nørskov, J. K. Improved adsorption energetics within density-functional theory using revised Perdew-Burke-Ernzerhof functionals. *Phys. Rev. B: Condens. Matter Mater. Phys.* **1999**, *59* (11), 7413−7421.

(51) Uribe-Romo, F. J.; Hunt, J. R.; Furukawa, H.; Klock, C.; O'Keeffe, M.; Yaghi, O. M. A crystalline imine-linked 3-D porous covalent organic framework. *J. Am. Chem. Soc.* **2009**, *131* (13), 4570−4571.

(52) Lin, S.; Diercks, C. S.; Zhang, Y.-B.; Kornienko, N.; Nichols, E. M.; Zhao, Y.; Paris, A. R.; Kim, D.; Yang, P.; Yaghi, O. M. Covalent organic frameworks comprising cobalt porphyrins for catalytic CO_2 reduction in water. *Science* **2015**, *349* (6253), 1208−1213.

(53) Wan, S.; Gándara, F.; Asano, A.; Furukawa, H.; Saeki, A.; Dey, S. K.; Liao, L.; Ambrogio, M. W.; Botros, Y. Y.; Duan, X.; et al. Covalent organic frameworks with high charge carrier mobility. *Chem. Mater.* **2011**, *23* (18), 4094−4097.

(54) Gong, Y.-N.; Zhong, W.; Li, Y.; Qiu, Y.; Zheng, L.; Jiang, J.; Jiang, H.-L. Regulating Photocatalysis by Spin-State Manipulation of Cobalt in Covalent Organic Frameworks. *J. Am. Chem. Soc.* **2020**, *142* (39), 16723−16731.

(55) Zitolo, A.; Ranjbar-Sahraie, N.; Mineva, T.; Li, J.; Jia, Q.; Stamatin, S.; Harrington, G. F.; Lyth, S. M.; Krtil, P.; Mukerjee, S.; Fonda, E.; Jaouen, F. Identification of catalytic sites in cobalt-nitrogen-carbon materials for the oxygen reduction reaction. *Nat. Commun.* **2017**, *8* (1), 957.

(56) Paulus, U.; Schmidt, T.; Gasteiger, H.; Behm, R. Oxygen reduction on a high-surface area Pt/Vulcan carbon catalyst: a thin-film rotating ring-disk electrode study. *J. Electroanal. Chem.* **2001**, *495* (2), 134−145.

(57) Shinagawa, T.; Garcia-Esparza, A. T.; Takanabe, K. Insight on Tafel slopes from a microkinetic analysis of aqueous electrocatalysis for energy conversion. *Sci. Rep.* **2015**, *5*, 13801.

(58) Viswanathan, V.; Hansen, H. A.; Rossmeisl, J.; Nørskov, J. K. Unifying the $2e^-$ and $4e^-$ reduction of oxygen on metal surfaces. *J. Phys. Chem. Lett.* **2012**, *3* (20), 2948−2951.

(59) Amiinu, I. S.; Liu, X.; Pu, Z.; Li, W.; Li, Q.; Zhang, J.; Tang, H.; Zhang, H.; Mu, S. From 3D ZIF nanocrystals to Co-N_x/C nanorod array electrocatalysts for ORR, OER, and Zn-air batteries. *Adv. Funct. Mater.* **2018**, *28* (5), 1704638.

(60) Siahrostami, S.; Björketun, M. E.; Strasser, P.; Greeley, J.; Rossmeisl, J. Tandem cathode for proton exchange membrane fuel cells. *Phys. Chem. Chem. Phys.* **2013**, *15* (23), 9326−9334.